Accepted Manuscript

Article

Electrochemical hydrogenation of mixed-phase TiO$_2$ nanotube arrays enables remarkably enhanced photoelectrochemical water splitting performance

Jiaqin Liu, Mengjia Dai, Jian Wu, Ying Hu, Qi Zhang, Jiewu Cui, Yan Wang, Hark Hoe Tan, Yucheng Wu

Article

Electrochemical hydrogenation of mixed-phase TiO$_2$ nanotube arrays enables remarkably enhanced photoelectrochemical water splitting performance

Jiaqin Liu*[acd], Mengjia Dai[ac], Jian Wu[ac], Ying Hu[ac], Qi Zhang[ac], Jiewu Cui[bc], Yan Wang[bc], Hark Hoe Tan[d], Yucheng Wu[*bc]

a Institute of Industry and Equipment Technology, Hefei University of Technology, Hefei 230009, China

b School of Materials Science and Engineering, Hefei University of Technology, Hefei 230009, China

c Key Laboratory of Advanced Functional Materials and Devices of Anhui Province, Hefei 230009, China

d Department of Electronic Materials Engineering, Research School of Physics and Engineering, The Australian National University, Canberra, ACT 2601, Australia

* Corresponding Author E-mails: jqliu@hfut.edu.cn (J. Liu), ycwu@hfut.edu.cn (Y. Wu)

Abstract: We first report that photoelectrochemical (PEC) performance of electrochemically hydrogenated TiO$_2$ nanotube arrays (TNTAs) as high-efficiency photoanodes for solar water splitting could be well tuned by designing and adjusting the phase structure and composition of TNTAs. Among various TNTAs annealed at different temperature ranging from 300 to 700℃, well-crystallized single anatase (A) phase TNTAs-400 photoanode shows the best photoresponse properties and PEC performance

due to the favorable crystallinity, grain size and tubular structures. After electrochemical hydrogenation (EH), anatase-rutile (A-R) mixed phase EH-TNTAs-600 photoanode exhibits the highest photoactivity and PEC performance for solar water splitting. Under simulated solar illumination, EH-TNTAs-600 achieves the best photoconversion efficiency of upeixed phases and intentionally introduced Ti^{3+} (oxygen vacancies) which enhances the photoactivity over both UV and visible-light regions, and boosts both charge separation and transfer efficiencies. These findings provide new insight and guidelines for the construction of highly efficient TiO_2-based devices for the application of solar water splitting.

Keywords: TNTAs; Electrochemical hydrogenation; Phase; Photoelectrochemical; Hydrogen generation

1. Introduction

With the depletion and pollution of fossil fuel, extensive studies have been carried out for clean and renewable energy. Hydrogen fuel generated from the two most abundant and free resources on this planet, which are sunlight and water, has attracted much attention as a prospective alternative fuel as it is clean and has high energy density. Since the discovery of hydrogen generation through water splitting over a TiO_2 photoanode in a photoelectrochemical (PEC) system by Fujishima and Honda [1], significant research [2-5] has been focusing on PEC water splitting using semiconductors as photoelectrode materials for converting solar energy into hydrogen energy. TiO_2 was regarded as the most promising material for photocatalytic applications due to its low cost, nontoxicity, superior photoactivity and photochemical stability. In particular, in comparison with other randomly oriented TiO_2 nanostructures, highly ordered anodic TiO_2 nanotube arrays (TNTAs) with well-defined tubular structures hold great promise and excellent efficiency as photoelectrode materials in PEC system owing to their high-surface-area, direct

pathway for electron transport, favorable reusability and facile fabrication [6-9].

Recently, hydrogenated TNTAs with intentionally introduced Ti^{3+} (oxygen vacancies) have been demonstrated to be a quite effective strategy for improving the electronic conductivity and photoresponse properties [6, 10-13]. Hydrogenation of TNTAs could be achieved via various methods such as hydrogen thermal treatment [14, 15], hydrogen plasma treatment [16, 17], electrochemical hydrogenation (EH) [18, 19] and chemical hydrogenation [20, 21]. Among various hydrogenation techniques, EH is a simple, low-cost and environment-friendly approach, overcoming the weakness of other hydrogenation methods such as high-energy consumption, expensive facility and complex process. Under an external electric field, hydrogen is driven into TiO_2 lattice and reduces Ti^{4+} to Ti^{3+} (oxygen vacancies). For instance, Zhang et al. [19] demonstrated that electrochemical hydrogenated TNTAs photoelectrode showed remarkably improved and stable water splitting performance, and the optimized saturation photocurrent density and photoconversion efficiency under AM 1.5G illumination were identified to be 2.8 mA cm^{-2} at 1.23 V vs. RHE (RHE, reversible hydrogen electrode) and 1.27% respectively. Our previous work [22] proved that in contrast to the pristine TNTAs, EH process considerably enhanced the electrical properties and electrochemical performance of TNTAs, which enabled EH-TNTAs to serve as an ideal current collector for constructing TNTA-based electrodes applied for high performance supercapacitors.

Moreover, TiO_2 commonly exists in three phases: anatase (A, tetragonal), rutile (R, tetragonal), and brookite (B, orthorhombic). By far, A and R phases are the most common phases synthesized and widely studied for the application as photocatalyst due to their ease of synthesis. On the other hand, B-phase is rarely studied due to the difficulties in synthesizing and thermodynamically metastability under ambient conditions. Compared with single phase TiO_2, mixed-phase TiO_2 (A-R in particular) has proven to have higher photocatalytic activities [23-25]. Since photocatalytic activity is restricted by the fast electron-hole recombination, through coupling with another type of photoactive

semiconductor material, charge transfer can occur, resulting in effective separation of photo-excited electrons from holes, and thus suppressing electron-hole recombination. A well-known example is commercial P25 powder with 75% A-phase and 25% R-phase. With illumination of UV-light on P25, photo-excited electrons from A-phase will be transferred to R-phase due to the lower conduction band energy of R-phase, and consequently inhibiting charge recombination. There has been some reported works regarding to whether & how the phase structure and composition affect the PEC performance of TiO_2 materials [23, 25-27]. However, to date there has been no relevant reports exploring whether & how the phase structure and composition affect the photoresponse properties of TiO_2 before and after EH treatment.

In this work, TNTAs with different phase structure and composition were prepared via electrochemical anodization followed by annealing crystallization. Then, hydrogenation of TNTAs was conducted using EH technique. Our results indicated that EH treatment remarkably enhanced the PEC water splitting performance of TNTAs. Surprisingly, in contrast to the single A-phase TNTAs-400 with best PEC water splitting performance among all TNTAs electrodes before EH process, A-R mixed-phase EH-TNTAs-600 showed the best PEC solar water splitting performance, well beyond that of other EH-TNTAs photoanodes. EH-TNTAs-600 achieves the best photoconversion efficiency of 1.52% and the highest H_2 generation rate of 40.4 μmol h^{-1} cm^{-2}. Further, the fundamental mechanism of phase-dependent improvement in PEC activity of EH-TNTAs photoelctrodes was fully explored. This work demonstrates that precisely designing and controlling the phase structure and composition of TNTAs could achieve maximum PEC performance of hydrogenated TNTAs, and thus provides theoretical insight and practical guidelines for the application of TiO_2-based electrode in the PEC water splitting.

2. Experimental

2.1 Preparation of TNTAs

Highly ordered and well-separated TNTAs were directly grown on a Ti foil (0.1 mm, 99.7%) using electrochemical anodization. Prior to anodization, Ti foils were ultrasonically cleaned in acetone, ethanol, and deionized water, respectively, for 20 min. Electrochemical anodization was performed on a two-electrode setup using a direct-current (DC) power supply at 60 V for 6 h in ice bath. A Ti foil was used as the working electrode, a graphite foil as the cathode, a solution of 0.25 mol L^{-1} NH_4F in ethylene glycol with 8 vol% H_2O as the electrolyte. After anodization, the as-fabricated amorphous TNTAs were annealed in air at different temperature ranging from 300 to 700℃ for 2 h with a heating rate of 2 ℃ min^{-1}. The as-prepared TNTAs sample was denoted as TNTAs-*T* (*T* refers to the annealing temperature).

2.2 Electrochemical hydrogenation of TNTAs

Electrochemical hydrogenation of TNTAs to obtain the EH-TNTAs was carried out in a two-electrode setup using a DC power supply at 4 V for 20 min at ambient temperature. The as-fabricated TNTAs-*T* was used as the cathode, a graphite foil as the anode, and an aqueous solution of 0.1 mol L^{-1} Na_2SO_4 as the electrolyte. Similarly, the resulting EH-TNTAs sample was denoted as EH-TNTAs-*T*.

2.3 Characterization

Morphologies and structure features of as-fabricated TNTAs samples were characterized using field-emission scanning electron microscope (FESEM, SU-8020, operated at 5.0 kV), transmission electron microscope (TEM, JEM-2100F, operated at 200 kV), X-ray diffractometer (XRD, Rigaku D/Max-2500V) and Raman spectroscopy (LabRAM HR Evolution). X-ray photoelectron spectroscopy (XPS) analysis was conducted on an ESCALAB 250Xi spectrometer with monochromated Al Kα radiation (1,486.6 eV). The electron paramagnetic resonance (EPR) spectra were recorded at 100 K using a Bruker EMX plus/X-band spectrometer. UV-vis diffuse reflectance spectra (DRS) were measured on a Shimadzu UV-3600 UV-vis-NIR spectrophotometer using $BaSO_4$ as a reference standard.

2.4 Photoelectrochemical measurement

All PEC measurements were carried out on an electrochemical workstation (CHI760E) in a three-electrode system using the tested sample, a Pt wire, an Ag/AgCl (3 mol L^{-1} KCl) electrode as the working, counter, and reference electrodes, respectively, and using 1 mol L^{-1} KOH aqueous solution as electrolyte. A 300 W xenon lamp (HSX-F300, NBeT Company) was utilized as the solar simulator (AM 1.5G, 100 mW cm^{-2}). The transient photocurrent response was evaluated under chopped light irradiation at an applied potential of 0 V (vs. Ag/AgCl). The linear sweep voltammetry (LSV) was carried out from -1.0 to 0.6 V (vs. Ag/AgCl) at a scan rate of 10 mV s^{-1}. The incident-photon-to-current-conversion efficiency (IPCE) was measured at an applied potential of 0 V (vs. Ag/AgCl) with the assistance of a motorized monochrometer. Electrochemical impedance spectroscopy (EIS) measurements were conducted in the frequency ranging from 100 mHz to 100 kHz at open-circuit potential with an amplitude of 5 mV. For the evaluation of charge separation (η_{sep}) and surface charge transfer (η_{trans}) efficiencies, LSV was measured in 1 mol L^{-1} KOH electrolyte with 0.2 mol L^{-1} Na_2SO_3 as hole scavenger.

   PEC solar water splitting was carried out in an Ar gas flow system. The amounts of evolved gases were determined by gas chromatography (Agilent, GC-7890B, Ar carrier). A 300 W Xe-lamp was still utilized as the light source. The electrolyte was bubbled with Ar before measurements to remove dissolved O_2.

3. Results and discussion

In order to identify the crystal structure and possible phase transition during annealing treatment and EH process, XRD spectra were first collected for both TNTAs fabricated at various annealing temperatures and their corresponding EH-TNTAs samples, as shown in Figs.1 and S1 (online). After subtracting the diffraction peaks from Ti foil, all diffraction peaks centered at 25.3°, 37.9°, 48.1° and 53.9° were observed in all TNTAs samples.

These peaks are well indexed to (101), (004), (200), and (105) planes of tetragonal A-phase TiO_2 (JCPDS No. 21-1272). Obviously, extra peaks at 27.3°, 36.5°, 41.4°, 44.2° and 54.5° appeared in the TNTAs-600 which could be ascribed to (110), (101), (111), (210) and (211) planes of tetragonal R-phase TiO_2 (JCPDS No. 21-1276), and the R-phase intensity increases with further increase of annealing temperature up to 700℃. Even so, peaks of A-phase are still dominant over the peaks of R-phase. Above XRD analysis demonstrates that amorphous TiO_2 transforms to pure A-phase upon thermal treatment at 500℃ or below, while TiO_2 phase transformation occurs from A to R phase at 600℃ or above. Amorphous TNTAs highly crystallized into A-phase rather than R-phase even with the annealing temperature of up to 700℃. Besides, XRD patterns of both TNTAs and EH-TNTAs samples show almost the same diffraction patterns, which means no phase transformation occurs during EH process.
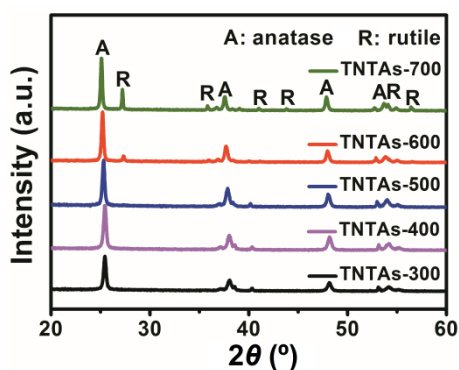

Fig.1 (Color online) XRD patterns of various TNTAs samples with different annealing temperatures (from bottom to top: 300, 400, 500, 600, 700℃).

Afterwards, Spurr and Scherrer equations [28] were utilized to calculate relative amounts of A and R phases as well as the mean crystallite sizes in various TNTAs samples based on the XRD data, as listed in Table S1 (online). Apparently, the average crystallite sizes of both A and R phases increase with the increase of crystallization temperature after the nucleation, mainly due to the higher energy to accelerate the growth of crystal grains. Moreover, as the crystallization temperature increased from 600 to

700℃, the crystallite sizes of both A and R phases increased, and the mass fraction of R-phase dramatically increased from 10.7% to 34.2%. XRD results clearly illustrate that the phase structure and composition of TNTAs could be easily and precisely tuned by adjusting the crystallization parameters.

The morphologies of both TNTAs and EH-TNTAs annealed from 300 to 700℃ are shown in Fig.2. The as-formed TiO_2 NTs in all samples have a uniform diameter of ~180 nm, a wall thickness of ~25 nm, and a length of ~10 μm (Fig.S2 online). The distinct difference to the conventional TNTAs is that the TiO_2 NTs are free-standing and well-separated from each other with intertube spaces ranging from 8 to 15 nm. The free spacing among the tubes allows for more exposed active surface as well as efficient mass transport. As for the TNTAs annealed at 300, 400 and 500℃ (Fig.2a-c), no great changes in the tubular structure and surface morphology of TiO_2 NTs were observed, indicating the favorable thermal stability of TNTAs. When the temperature was raised up to 600℃ (Fig.2d), the tube walls became rough and began to rupture with tiny pores appearing in the tube walls, which could be clearly observed by TEM (Fig.3b). However, when the temperature was further increased up to 700℃ (Fig.2e), the tube walls began to collapse and the tubular structure was partially destroyed, which is attributed to the higher density of R-phase and extensive transformation from A to R phase as well as the rapid growth of R-phase grains at high temperature [29]. Moreover, EH-TNTAs samples (Fig.2f-j) display no distinct differences in tubular structure and surface morphology compared to their corresponding TNTAs counterparts. Notably, EH-TNTAs present a dark blue color versus the grey TNTAs due to the Ti^{3+} (oxygen vacancies) formation with an according change in the electronic and optical properties of the material.
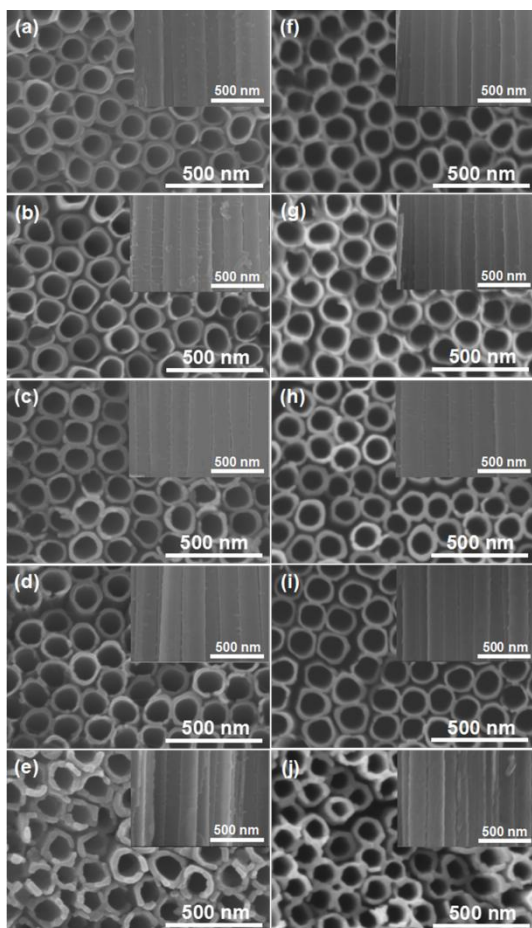
Fig. 2 FESEM images of various TNTAs (a-e) and EH-TNTAs (f-j) samples with different annealing temperatures (from top to bottom: 300, 400, 500, 600, 700℃)
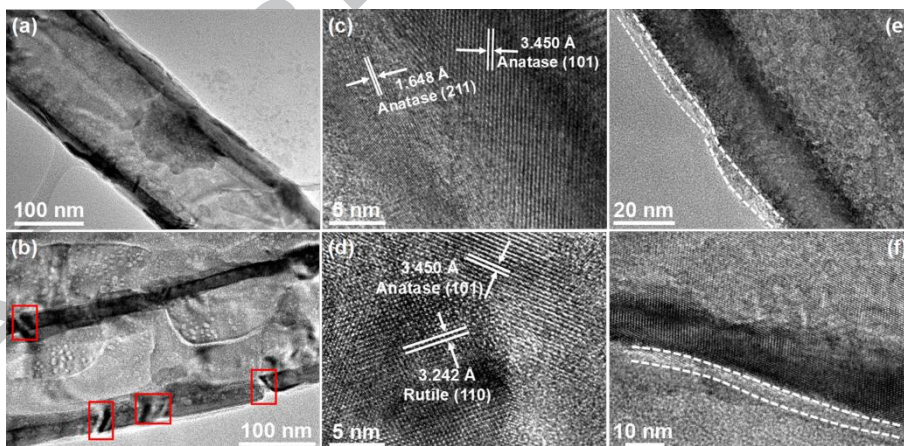

Fig. 3 (Color online) TEM images of TNTAs-400 (a) and TNTAs-600 (b). HRTEM images of TNTAs-400 (c), TNTAs-600 (d), EH-TNTAs-400 (e) and EH-TNTAs-600 (f).

Since the following characterizations and measurements indicate that among various TNTAs and EH-TNTAs samples, TNTAs-400 and EH-TNTAs-600 exhibit the best photoactivity and PEC performance before and after EH treatment respectively. The microstructure features of these two samples are relatively typical and comparable. Thus, more attention will be focused on the two representative samples in the following discussion.

Microstructures and morphologies of TNTAs-400 and EH-TNTAs-600 were further observed using TEM, as illustrated in Fig.3. Comparing to the smooth tube walls of TNTAs-400 (Fig.3a), tube walls of TNTAs-600 became rough, and large numbers of tiny pores marked with small boxes could be clearly observed in the walls (Fig.3b), which is in good agreement with SEM analysis. Well resolved lattice fringes of d = 3.45 and 1.648 Å observed from TNTAs-400 (Fig.3c) are identified to be the (101) and (211) planes of A-phase TiO_2. As for TNTAs-600 (Fig.3d), within tens of nanometers range, two neighboring and different lattice fringes of d = 3.45 and 3.24 Å correspond respectively to A-phase (101) and R-phase (110), clearly confirming the A-R mixed phase structure for TNTAs-600. Besides, after EH well-defined surface edges of TiO_2 NTs become blurred (marked area with dotted lines in Fig.3e, f), which indicate the distortion of TiO_2 lattice structures induced by large numbers of surface introduced Ti^{3+} (oxygen vacancies). Thus, both SEM and TEM observations were in good accordance with former XRD results.

XPS and Raman spectroscopy were conducted to reveal the variation of the chemical composition and coordination structure of TNTAs during annealing treatment and EH process, as clearly shown in Fig.4. Five Raman characteristic peaks at around 145.0, 198.4, 397.3, 517.3 and 639.1 cm^{-1} in all TNTAs samples (Fig.4a) are assigned to the $E_g(1)$, $E_g(2)$, B_{1g}, A_{1g}/B_{2g} and $E_g(3)$ mode of A-phase TiO_2 [30]. By comparison, two additional peaks at 445.3 and 613.2 cm^{-1} were observed for TNTAs-600 and became stronger for TNTAs-700, which are ascribed to the formation and growth of R-phase TiO_2

[31], well confirming the XRD results. Further, as the crystallization temperature increases from 300 to 700℃, the frequency of the strongest $E_g(1)$ mode shifted from 146.95 to 144.21 cm^{-1}, and the $E_g(1)$ peak intensity gradually increased (Fig.4a), which could be ascribed to the phonon dispersion away from the center of the brillouin zone and the growth in crystallite size [31, 32]. Compared to the TNTAs samples, a slight blueshift and broadening of the strongest $E_g(1)$ peak are observed in the corresponding EH-TNTAs samples (Fig.4b), suggesting the increased surface disorder due to the intentionally introduced Ti^{3+} (oxygen vacancies) [33]. Fig.4c compares the normalized Ti 2p core level XPS spectra of TNTAs-400 (black curve) and EH-TNTAs-400 (red curve), together with their difference spectrum. Two peaks centered at 459.13 and 465.48 eV that correspond to the Ti $2p_{3/2}$ and Ti $2p_{1/2}$ peaks of Ti^{4+} in TiO_2 are observed for both samples. In contrast to TNTAs-400, both Ti $2p_{1/2}$ and Ti $2p_{3/2}$ peaks for EH-TNTAs-400 exhibit a slight redshift, indicating that they have different bonding environments. By subtracting the normalized Ti 2p spectra of EH-TNTAs-400 with TNTAs-400, two extra peaks centered at 458.48 and 463.78 eV are clearly observed. These two peaks are attributed to the characteristic Ti $2p_{3/2}$ and Ti $2p_{1/2}$ peaks of Ti^{3+}, proving the generation of Ti^{3+} sites (oxygen vacancies) during EH process [34-36]. Similar result could be obtained from the Ti 2p XPS spectra for TNTAs-600 and EH-TNTAs-600 as well (Fig.4d). More importantly, the binding energy of both Ti $2p_{3/2}$ and Ti $2p_{1/2}$ for EH-TNTAs-600 are slightly lower than that of EH-TNTAs-400, and relative intensity of Ti^{3+} peaks for EH-TNTAs-600 is obviously higher than that of EH-TNTAs-400, revealing that more Ti^{3+} sites (oxygen vacancies) were introduced and stabilized in the EH-TNTAs-600 in contrast to EH-TNTAs-400.
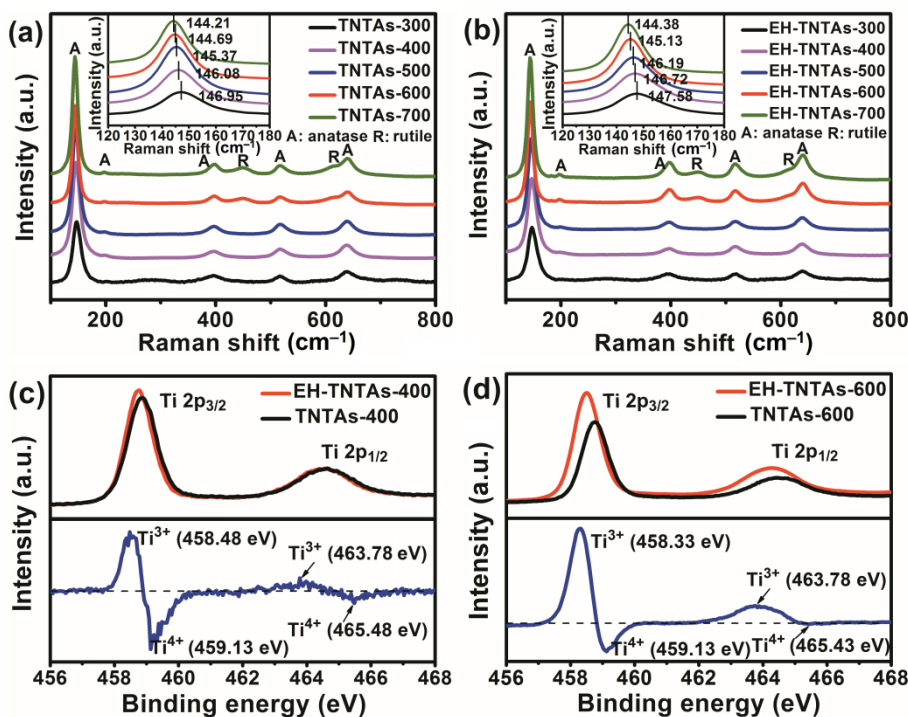
Fig. 4 Raman spectra of both TNTAs (a) and EH-TNTAs (b) with different annealing temperatures, insets are the magnification of $E_g(1)$ peak. (c) Ti 2p XPS spectra of TNTAs-400 and EH-TNTAs-400. (d) Ti 2p XPS spectra of TNTAs-600 and EH-TNTAs-600.

EPR is a sensitive and effective method for detecting Ti^{3+}. In this work, EPR testing was conducted to support the formation of Ti^{3+} (oxygen vacancies) in EH-TNTAs samples. Fig.5 compares the EPR spectra of EH-TNTAs-400, EH-TNTAs-600 as well as their unhydrogenated counterparts, TNTAs-400 and TNTAs-600. As can be clearly seen, TNTAs-400 and TNTAs-600 do not show any paramagnetic signal, whereas both EH-TNTAs-400 and EH-TNTAs-600 exhibit a strong EPR signal at $g \approx 1.94$, which can be assigned to the paramagnetic Ti^{3+} species [37]. More significantly, the signal intensity of Ti^{3+} for EH-TNTAs-600 is apparently higher than that of EH-TNTAs-400, suggesting that more Ti^{3+} centers are created and stabilized in the A-R mixed phase EH-TNTAs-600 in comparison to single A-phase EH-TNTAs-400. This is in good agreement with the result of XPS analysis. Moreover, both EH-TNTAs-400 and EH-TNTAs-600 also present a paramagnetic signal at $g \approx 2.001$ for oxygen vacancies, proving the presence of oxygen

vacancies associated with surface Ti^{3+} [38]. It is accepted that the surface Ti^{3+} centers can trap atmospheric O_2 to generate $\cdot O_2^-$ with an EPR signal at $g \approx 2.02$ [39]. Thus, EPR data confirm that Ti^{3+} (oxygen vacancies) is created during EH process and exists both in the bulk and on the surface.
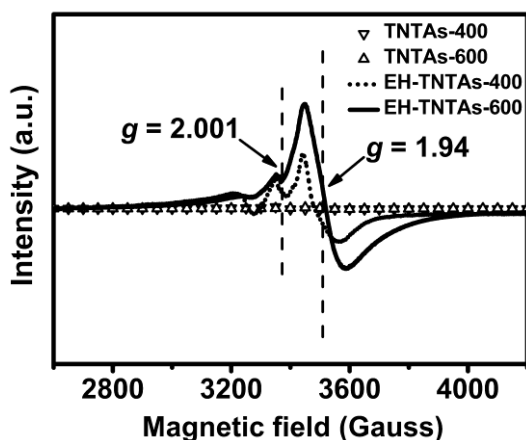

Fig. 5 (Color online) EPR spectra for TNTAs-400, TNTAs-600, EH-TNTAs-400 and EH-TNTAs-600.

To investigate photoresponse properties of various TNTAs electrodes, the PEC measurement was carried out in a three-electrode cell under illumination in 1 mol L^{-1} KOH electrolyte. The plots of transient photocurrent response vs. time for various TNTAs and EH-TNTAs electrodes under simulated solar illumination (100 mW cm^{-2}) are shown in Fig.6a, b respectively. All TNTAs show good photoresponses under conditions of light on-off cycles, which indicates the rapid charge transportation process from the walls of TiO_2 NTs to Ti substrate. Without illumination, the current values are almost zero while the photocurrents rapidly rise to a stable value upon illumination, which are reproducible for several on-off cycles. The observed photocurrents are derived from the photo-excited electrons of TNTAs photoanodes. Among various TNTAs electrodes (Fig.6a), photocurrent first rises and then falls with increase of annealing temperature, and well-crystallized single A-phase TNTAs-400 yields the highest photocurrent density of 1.48 mA cm^{-2} due to the favorable crystallization, grain size and tubular structures. With further increase of temperature, the photocurrent gradually decreases owing to the grain

growth, decrease of A-phase fraction caused by A-to-R phase transformation and the destruction of tubular structures. Transient photocurrent responses of various TNTAs electrodes demonstrate that phase structures and crystallization can remarkably affect the photoresponse properties of TNTAs. After EH process, as can be seen in Fig.6b, the photocurrents of EH-TNTAs electrodes are distinctly higher than their corresponding TNTAs electrodes. Besides, the photocurrents of EH-TNTAs rise with increase of annealing temperature, only the photocurrent of EH-TNTAs-700 slightly decreases, and thereby the mixed phase EH-TNTAs-600 yields the highest photocurrent density of 2.74 mA cm^{-2}, well beyond that of other EH-TNTAs electrodes. Transient photocurrent responses of various TNTAs electrodes reveal that EH can significantly enhance the photoresponse properties of TNTAs by the introduction of substantial Ti^{3+} (oxygen vacancies). However, the improvement extent varies greatly with the phase structures and crystallization of TNTAs, and the improvement for A-R mixed phase EH-TNTAs-600 before and after EH treatment is maximum (Fig.S3 online).
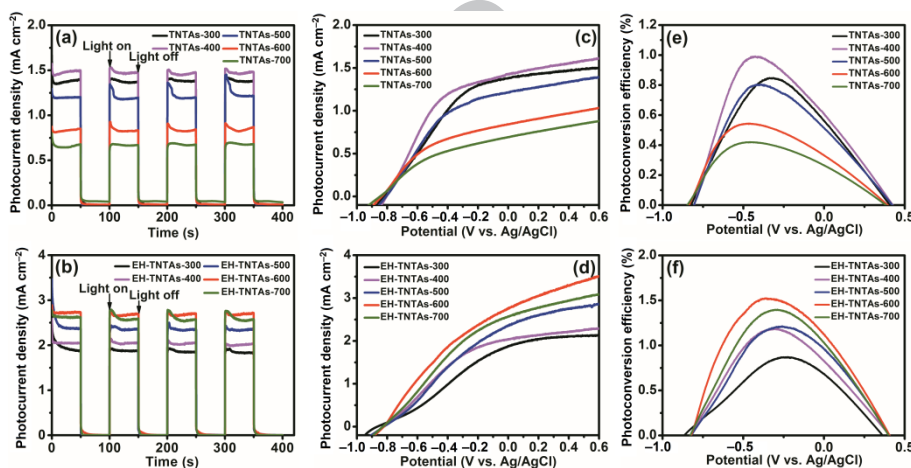
Fig.6 Transient photocurrent responses (a, b), linear sweep voltammograms (c, d) and photoconversion efficiencies (e, f) of various TNTAs and EH-TNTAs under simulated solar illumination (100 mW cm^{-2}).

Additionally, transient photocurrent responses of various TNTAs electrodes under visible-light illumination were further conducted, as shown in Fig.S4 (online). Overall,

the photocurrents of EH-TNTAs are greater than that of their corresponding TNTAs electrodes, but the photocurrents for all TNTAs electrodes under visible-light illumination are much lower than their respective photocurrents obtained under simulated solar light illumination, and thus could be almost negligible. UV-vis DRS measurements also confirm that all TNTAs and EH-TNTAs samples exhibit strong absorption in UV light region (Fig.S5a (online) and Fig. 5b). No significant absorption could be detected in visible-light region due to the intrinsic wide band gap of TiO_2 (3.20 eV). And for TNTAs-600, TNTAs-700 and their counterparts EH-TNTAs-600 and EH-TNTAs-700, obvious absorption in visible-light region can be clearly observed owing to A-to-R phase transformation and increase of R-phase fraction. Thus, photocurrent responses for all TNTAs and EH-TNTAs electrodes under visible light illumination are relatively weak. Further comparison between individual TNTAs and its corresponding EH-TNTAs (Fig.S5c-e (online) and Fig.7) clearly indicates that the intentionally introduced Ti^{3+} (oxygen vacancies) during the EH process indeed has an impact on the optical properties of TiO_2 nanotubes. In contrast to pristine TNTAs, the absorption edge of its corresponding EH-TNTAs exhibits an obvious red-shift, and thus contributing to higher photocurrent responses for EH-TNTAs with visible-light illumination.
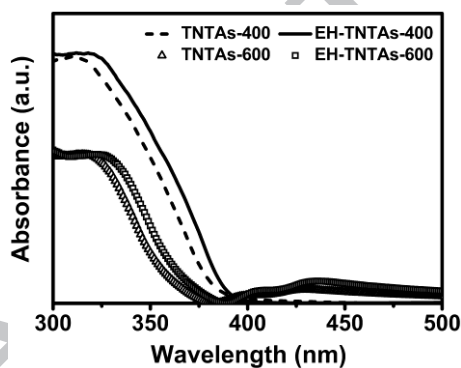

Fig.7 UV-vis diffuse reflectance spectra of TNTAs-400, TNTAs-600, EH-TNTAs-400 and EH-TNTAs-600.

Then, LSV curves of all TNTAs photoanodes (Fig.6c, d) were measured at 10 mV·s^{-1} from -1.0 to 0.6 V (vs. Ag/AgCl), and their corresponding photoconversion efficiencies η (Fig.6e, f) were calculated via the equation (1) [40]:

$$\eta(\%) = j_{p}[\frac{E_{rev}^{0} - |E_{app}|}{I_0}] \times 100\% \quad , \quad (1)$$

where j_{p} is the photocurrent density (mA cm^{-2}), I_0 is the power density of incident light (mW cm^{-2}), E_{rev}^{0} is the standard reversible potential of 1.23 V (vs. NHE), and applied bias potential $E_{app}=E_{meas}-E_{aoc}$, where E_{meas} is the electrode potential (vs. Ag/AgCl) of working electrode at which photocurrent was measured under illumination, and E_{aoc} is electrode potential (vs. Ag/AgCl) of working electrode under open circuit condition when the photocurrent becomes zero. Before EH treatment, well-crystallized single A-phase TNTAs-400 yields the highest photoconversion efficiency of 0.98% at -0.47 V (vs. Ag/AgCl). While after EH process, A-R mixed phase EH-TNTAs-600 could achieve the best photoconversion efficiency of up to 1.52% at -0.42 V (vs. Ag/AgCl), which is substantially higher than EH-TNTAs-400. Besides, the photoconversion efficiencies of EH-TNTAs are remarkably enhanced in comparison to that of their corresponding TNTAs photoelectrodes.

IPCE provides a reliable technique to evaluate the wavelength dependent photoresponse of photoelectrodes. IPCE can be expressed using the following equation [41]:

$$IPCE = \frac{1240I}{\lambda J_{light}} \quad , \quad (2)$$

Where λ is the incident light wavelength, I and J_{light} is photocurrent density and incident light irradiance at a specific wavelength, respectively. In comparison to the TNTAs annealed at 400 and 600℃, the corresponding EH-TNTAs-400 and EH-TNTAs-600 exhibit significantly enhanced photoactivity over the entire UV region (Fig.8a), which implies that the photogenerated carriers are more efficiently separated and transported in

the EH-TNTAs than in the pristine TNTAs. Further, A-R mixed phase EH-TNTAs-600 exhibits the highest IPCE value of around 90% in full UV region with a maximum value of 92% at 360 nm, and presents photoactivity enhancement within the visible-light region (400-500 nm) as well. This is ascribed to the synergy of R-phase (E_g=3.0 eV) formation and Ti^{3+} (oxygen vacancies) generation during EH process, and in good agreement with the extended absorption in the DRS spectra and the increased visible-light photocurrent. To gain deeper insight into the charge transfer properties associated with photoelectrodes, EIS measurements were subsequently performed at open circuit potential with amplitude of 5 mV under illumination. Figs.8b and S6 (online) illustrate the Nyquist plots of tested TNTAs and EH-TNTAs photoelectrodes. For quantitative analysis, experimental data of impedance spectra were fitted to the model depicted by the equivalent circuit (insets in Fig. 8b). In this model, R_s is the solution resistance, R_{ct} and R_c represent the inherent resistance of the working electrode and charge transfer resistance through the electrolyte respectively, the constant phase elements (CPE_1 and CPE_2) refer to the real double-layer capacitance. Table S2 (online) lists the fitted parameter values for various TNTAs and EH-TNTAs electrodes. It is obvious that EH-TNTAs show much lower impedance values than the corresponding TNTAs electrodes. This evident decline in the resistance of EH-TNTAs electrodes can be attributed to the greatly improved conductivity of electrode and efficient charge transport induced by the introduction of large numbers of Ti^{3+} (oxygen vacancies) during the EH process. Among various TNTAs electrodes, well-crystallized single A-phase TNTAs-400 has the lowest R_{ct} of 10.71 Ω. This reveals that favorable crystallization, grain size and tubular structures enable high charge transfer ability and conductivity, and thus contribute to the enhancement in photocurrent. After EH process, EH-TNTAs-600 yields the lowest R_{ct} of 4.17 Ω, much lower than that of other EH-TNTAs electrodes, which indicates that synergy of A-R mixed phases and introduction of oxygen vacancies greatly reduce the charge transfer resistance and

facilitate the charge carrier transport, and consequently boost the photocurrent significantly.
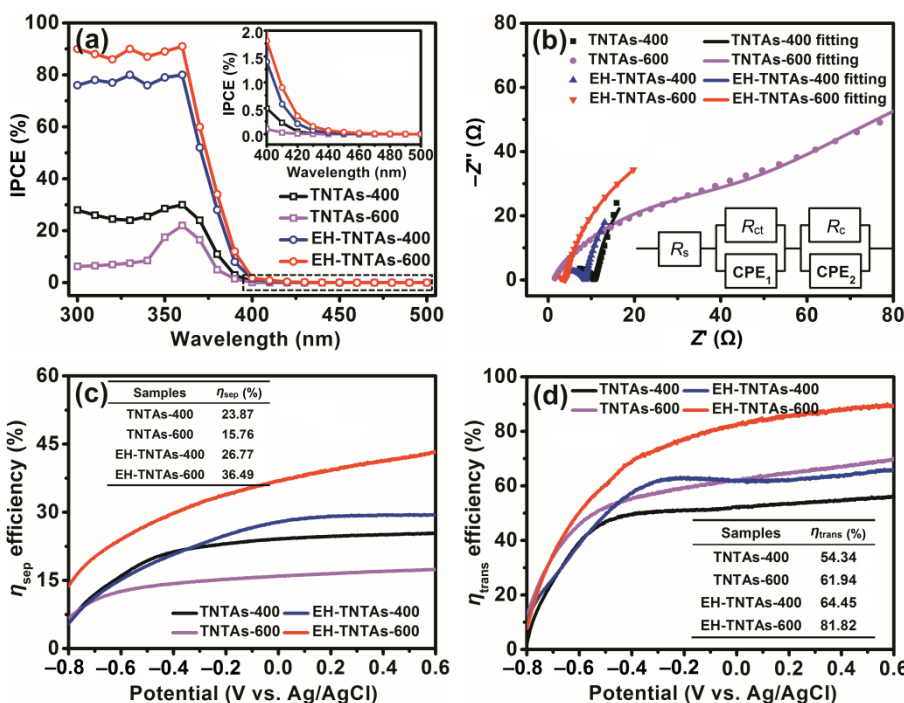

Fig. 8 (Color online) IPCE spectra (a), Nyquist plots (b), charge separation (η_{sep}) (c) and surface charge transfer (η_{trans}) (d) efficiencies of TNTAs-400, TNTAs-600, EH-TNTAs-400 and EH-TNTAs-600 photoelectrodes. The insets are the magnified view of IPCE spectra in visible-light region, equivalent circuit, charge separation and surface charge transfer efficiencies at 0 V (vs. Ag/AgCl), respectively.

To further explore the fundamental mechanism of phase-dependent improvement in PEC activity of EH-TNTAs photoelctrodes, charge separation (η_{sep}) and surface charge transfer (η_{trans}) efficiencies were investigated using Na_2SO_3 as the hole scavenger [42], as shown in Fig.8c, d. With the assumption that η_{trans} is 100% with Na_2SO_3 in the electrolyte [43], the η_{trans} could be estimated by calculating the photocurrent ratio measured without/with Na_2SO_3. Similarly, the η_{sep} can be estimated by dividing the photocurrent density with unity converted photocurrent densities (J_{abs}). J_{abs} can be calculated by integrating the corresponding UV-vis DRS curves (Fig.S5 online) with the standard solar spectrum (Fig.S7 online). Detailed calculation, J_{abs} (Fig.S8 online) and LSV curves (Fig.S9 online) of TNTAs-400, TNTAs-600 and their corresponding EH-TNTAs-400 and

EH-TNTAs-600 photoanodes measured with presence of Na_2SO_3 can be found in supporting information (online). Obviously, EH-TNTAs-400 and EH-TNTAs-600 exhibit much higher η_{sep} and η_{trans} than their corresponding TNTAs photoanodes, indicating that EH treatment significantly enhances not only surface charge transfer but also charge separation. Especially, A-R mixed phase EH-TNTAs-600 brings out the maximum improvement with η_{sep} and η_{trans}, which contribute to its best photoactivity and PEC performance.

Figs.9a and S10 (online) compare the PEC H_2 generation rate of various TNTAs and EH-TNTAs photoanodes. It is evident that EH significantly enhances the H_2 generation rate of TNTAs, and the extent of enhancement varies with the phase structure and crystallization of TNTAs. Among all EH-TNTAs photoanodes, EH-TNTAs-600 achieves the highest H_2 generation rate of 40.4 $\mu mol\ h^{-1}\ cm^{-2}$. The results of PEC H_2 generation measurements well match that of above photocurrent response tests. Moreover, the photocurrent densities of TNTAs-400 and TNTAs-600 as well as their corresponding EH-TNTAs photoanodes (Fig.9b) remain constant over 4 h illumination, revealing the prominent stability of TNTAs photoanode for H_2 generation by solar water splitting.
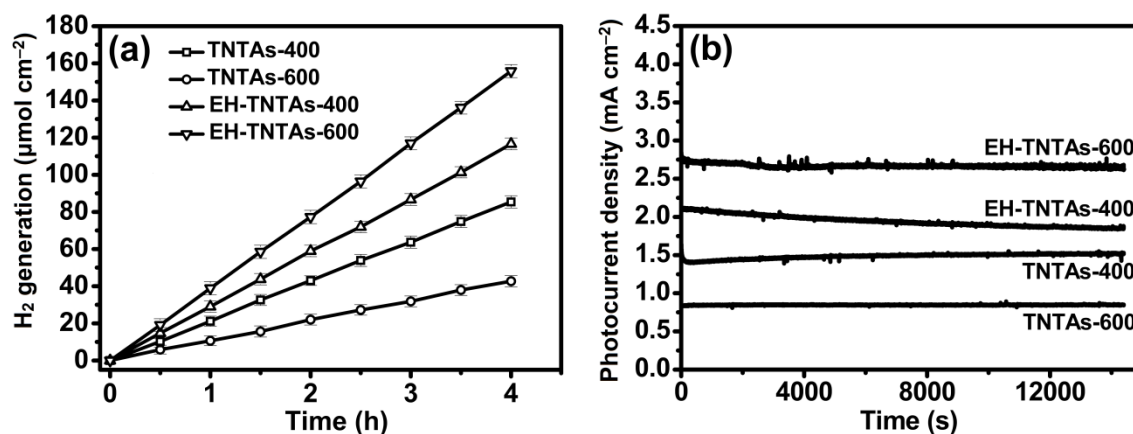
Fig. 9 Measured H_2 generation (a) and photocurrent-time profiles (b) as a function of time for TNTAs-400, TNTAs-600, EH-TNTAs-400 and EH-TNTAs-600 electrodes at 0 V vs. Ag/AgCl, in a 1 mol L^{-1} KOH solution under 100 mW cm^{-2} illumination.

4. Conclusions

In summary, this work first demonstrates that the PEC performance of electrochemical hydrogenated TNTAs for solar water splitting could be well tuned by designing and adjusting the phase structure and composition of TNTAs. Among various TNTAs annealed at different temperature ranging from 300 to 700℃, well-crystallized single A-phase TNTAs-400 photoanode shows the best photoresponse properties and PEC performance due to the favorable crystallinity and tubular structures. After EH treatment, A-R mixed phase EH-TNTAs-600 photoanode exhibits the highest photoactivity and PEC performance for solar water splitting, well beyond that of other EH-TNTAs photoanodes. This could be ascribed to the synergy of A-R mixed phases and intentionally introduced Ti^{3+} (oxygen vacancies) which enhances the photoactivity in both UV and visible-light regions and boosts charge separation and transfer efficiencies, thereby enabling remarkably enhanced PEC water splitting performance. This work has great theoretical and practical significance for designing and fabricating the TiO_2-based photoelectrodes in application of PEC solar water splitting.

Acknowledgments

Conflict of Interest: The authors declare that they have no conflict of interest.

Reference:

[1] Fujishima A, Honda K. Electrochemical photolysis of water at a semiconductor electrode. Nature 1972;238:37-38.

[2] Pu YC, Wang GM, Chang KD, et al. Au Nanostructure-decorated TiO_2 nanowires exhibiting photoactivity across entire UV-visible region for photoelectrochemical water splitting. Nano Lett. 2013;13:3817-3823.

[3] Kumar DP, Reddy NL, Karthik M, et al. Solar light sensitized p-Ag_2O/n-TiO_2 nanotubes heterojunction photocatalysts for enhanced hydrogen production in aqueous-glycerol solution. Sol Energy Mater Sol Cells 2016;154:78-87.

[4] Ahmad H, Kamarudin SK, Minggu LJ, et al. Hydrogen from photo-catalytic water splitting process: a review, Renew Sustain Energy Rev 2015;43:599-610.

[5] Wang Q, Hisatomi T, Jia QX, et al. Scalable water splitting on particulate photocatalyst sheets with a solar-to-hydrogen energy conversion efficiency exceeding 1%. Nat Mater 2016;15:611-615.

[6] Cui HL, Zhao W, Yang CY, et al. Black TiO_2 nanotube arrays for high-efficiency photoelectrochemical water-splitting. J Mater Chem A 2014;2:8612-8616.

[7] Zhang ZH, Wang P. Optimization of photoelectrochemical water splitting performance on hierarchical TiO_2 nanotube arrays, Energy Environ Sci 2012;5:6506-6512.

[8] Ye MD, Gong JJ, Lai YK, et al. High-efficiency photoelectrocatalytic hydrogen generation enabled by palladium quantum dots-sensitized TiO_2 nanotube arrays. J Am Chem Soc 2012;134:15720-15723.

[9] Qorbani M, Naseri N, Moradlou O, et al. How CdS nanoparticles can influence TiO_2 nanotube arrays in solar energy applications? Appl Catal B Environ. 2015;162:210-216.

[10] Chen XB, Liu L, Yu PY, et al. Increasing solar absorption for photocatalysis with black hydrogenated titanium dioxide nanocrystals. Science 2011;331:746-750.

[11] Dong JY, Han J, Liu YS, et al. Defective black TiO_2 synthesized via anodization for visible-light photocatalysis. ACS Appl Mater Interfaces 2014;6:1385-1388.

[12] Huo JC, Hu YJ, Jiang H, et al. In situ surface hydrogenation synthesis of Ti^{3+} self-doped TiO_2 with enhanced visible light photoactivity. Nanoscale 2014;6:9078-9084.

[13] Jiang XD, Zhang YP, Jiang J, et al. Characterization of oxygen vacancy associates within hydrogenated TiO_2: a positron annihilation study. J Phys Chem C 2012;116 :22619-22624.

[14] Liu N, Schneider C, Freitag D, et al. Black TiO_2 nanotubes: cocatalyst-free open-circuit hydrogen generation. Nano Lett 2014;14:3309-3313.

[15] Wang GM, Wang HY, Ling YC, et al. Hydrogen-treated TiO_2 nanowire arrays for photoelectrochemical water splitting. Nano Lett 2011;11:3026-3033.

[16] Kim HJ, Kim J, Hong B. Effect of hydrogen plasma treatment on nano-structured TiO_2 films for the enhanced performance of dye-sensitized solar cell. Appl Surface Sci 2013;274:171-175.

[17] Li X, Zhao JB, Sun SG, et al. The application of plasma treatment for Ti^{3+} modified TiO_2 nanowires film electrode with enhanced lithium-storage properties. Electrochim Acta 2016;211:395-403.

[18] Kim C, Kim S, Hong SP, et al. Effect of doping level of colored TiO_2 nanotube arrays fabricated by electrochemical self-doping on electrochemical properties. Phys Chem Chem Phys 2016;18:14370-14375.

[19] Zhang ZH, Hedhili MN, Zhu HB, et al. Electrochemical reduction induced self-doping of Ti^{3+} for efficient water splitting performance on TiO_2 based photoelectrodes. Phys Chem Chem Phys 2013;15:15637-15644.

[20] Kang Q, Cao JY, Zhang YJ, et al. Reduced TiO_2 nanotube arrays for photoelectrochemical water splitting. J Mater Chem A 2013;1:5766-5774.

[21] Fang WZ, Xing MY, Zhang JL. A new approach to prepare Ti^{3+} self-doped TiO_2 via $NaBH_4$ reduction and hydrochloric acid treatment. Appl Catal B Environ. 2014;160-161:240-246.

[22] Liu JQ, Xu J, Wang Y, et al. Electrochemical hydrogenated TiO_2 nanotube arrays decorated with 3D cotton-like porous MnO_2 enables superior supercapacitive performance. RSC Adv 2017;7:31512-31518.

[23] Yu JG, Wang B. Effect of calcination temperature on morphology and photoelectrochemical properties of anodized titanium dioxide nanotube arrays. Appl Catal B Environ 2010;94:295-302.

[24] Liu Y, Mu KS, Zhang YZ, et al. Facile synthesis of a narrow-gap titanium dioxide anatase/rutile nanofiber film on titanium foil with high photocatalytic activity under sunlight. Int J Hydrogen Energy 2016;41:10327-10334.

[25] Yang JS, Liao WP, Wu JJ. Morphology and interfacial energetics controls for hierarchical anatase/rutile TiO_2 nanostructured array for efficient photoelectrochemical water splitting. ACS Appl Mater Interfaces 2013;5:7425-7431.

[26] Cao FR, Xiong J, Wu FL, et al. Enhanced photoelectrochemical performance from rationally designed anatase/rutile TiO_2 heterostructures. ACS Appl Mater Interfaces 2016;8:12239-12245.

[27] Su R, Bechstein R, Sø L, et al. How the anatase-to-rutile ratio influences the photoreactivity of TiO_2. J Phys Chem C 2011;115:24287-24292.

[28] Schulte KL, DeSario PA, Gray KA. Effect of crystal phase composition on the reductive and oxidative abilities of TiO_2 nanotubes under UV and visible light. Appl Catal B Environ 2010;97:354-360.

[29] Sun Y, Yan KP, Wang GX, et al. Effect of annealing temperature on the hydrogen production of TiO_2 nanotube arrays in a two-compartment photoelectrochemical cell. J Phys Chem C 2011;115:12844-12849.

[30] Wu WL, Zhang ZH. Defect-engineered TiO_2 nanotube photonic crystals for the fabrication of near-infrared photoelectrochemical sensor. J Mater Chem B 2017;5:4883-4889.

[31] Sahoo S, Arora AK, Sridharan V. Raman line shapes of optical phonons of different symmetries in anatase TiO_2 nanocrystals. J Phys Chem C 2009;113:16927-16933.

[32] Rambabu Y, Jaiswal M, Roy SC. Effect of annealing temperature on the phase transition, structural stability and photo-electrochemical performance of TiO_2 multi-leg nanotubes. Catal Today 2016;278:255-261.

[33] Wang Z, Yang CY, Lin TQ, et al. Visible-light photocatalytic, solar thermal and photoelectrochemical properties of aluminium-reduced black titania. Energy Environ Sci 2013;6:3007-3014.

[34] Zhou H, Zhang YR. Enhancing the capacitance of TiO_2 nanotube arrays by a facile cathodic reduction process. J Power Sources 2013;239:128-131.

[35] Pei ZX, Zhu MS, Huang Y, et al. Dramatically improved energy conversion and storage efficiencies by simultaneously enhancing charge transfer and creating active sites in MnO_x/TiO_2 nanotube composite electrodes. Nano Energy 2016;20:254-263.

[36] Lu XH, Wang GM, Zhai T, et al. Hydrogenated TiO_2 nanotube arrays for supercapacitors. Nano Lett 2012;12:1690-1696.

[37] Zhou Y, Chen CH, Wang NN, et al. Stable Ti^{3+} self-doped anatase-rutile mixed TiO_2 with enhanced visible light utilization and durability. J Phys Chem C 2016;120:6116-6124.

[38] Liu X, Gao SM, Xu H, et al. Green synthetic approach for Ti^{3+} self-doped TiO_{2-x} nanoparticles with efficient visible light photocatalytic activity. Nanoscale 2013;5:1870-1875.

[39] Zuo F, Wang L, Wu T, et al. Self-doped Ti^{3+} enhanced photocatalyst for hydrogen production under visible light. J Am Chem Soc 2010;132:11856-11857.

[40] Li Z, Chen Y, Shen J, et al. Facile synthesis of heterogeneous Li_2TiO_3/TiO_2 nanocomposite with enhanced photoelectrochemical water splitting. New J Chem 2017;41:6305-6314.

[41] Tong XL, Yang P, Wang YW, et al. Enhanced photoelectrochemical water splitting performance of TiO_2 nanotube arrays coated with an ultrathin nitrogen-doped carbon film by molecular layer deposition. Nanoscale 2014;6:6692-6700.

[42] Li ZS, Luo WJ, Zhang ML, et al. An electrochemically treated $BiVO_4$ photoanode for efficient photoelectrochemical water splitting. Energy Environ Sci 2013;6:347-370.

[43] Wang SC, Chen P, Yun JH, et al. An electrochemically treated $BiVO_4$ photoanode for efficient photoelectrochemical water splitting. Angew Chem 2017;129:8620-8624.

Graphical abstract